*Materials Science-Poland, 37(4), 2019, pp. 607-614*
*http://www.materialsscience.pwr.wroc.pl/*
*DOI: 10.2478/msp-2019-0076*

# Photoluminescence and piezoelectricity investigation of $La_{1.98}Nd_{0.02}Ti_2O_7$, $Sm_{1.98}Ce_{0.02}Ti_2O_7$ and $Er_{1.98}Gd_{0.02}Ti_2O_7$ multifunctional materials

ESRA ÖZTÜRK*, EBRU SARILMAZ

Karamanoğlu Mehmetbey University, Faculty of Engineering, Department of Metallurgy and Materials Engineering, Karaman, Turkey

$Nd^{3+}$ doped $La_2Ti_2O_7$, $Ce^{4+}$ doped $Sm_2Ti_2O_7$ and $Gd^{3+}$ doped $Er_2Ti_2O_7$ have been synthesized at different reaction temperatures using solid state reaction method, and characterized using X-ray diffraction (XRD), scanning electron microscopy (SEM), differential thermal analysis (DTA), thermogravimetric analysis (TG). Excitation spectra, emission spectra and decay time curves of the samples were investigated by photoluminescence spectrophotometer (PL) and typical transitions of rare earth ions were observed. Dielectric properties, piezoelectric properties and Curie temperature of the obtained luminescent materials were measured for electrical characterization. The results showed that all materials have both photoluminescent and piezoelectric properties and show high Curie temperature.

Keywords: *multi-functional smart material; titanates; photoluminescent material; piezoelectric material*

## 1. Introduction

$RE_2Ti_2O_7$ type titanates have cubic pyrochlore crystal structure or monoclinic crystal structure of perovskite type. The crystal structure depends on the ionic radii of $RE^{3+}$ ions (RE = trivalent rare earth ions) [1, 2]. The rare earth titanates with $RE^{3+}$ ions having radii larger than $Sm^{3+}$ form structures of perovskite type while with other rare earth ions with smaller radii they form cubic pyrochlore type structures. Thus, it is expected that $Sm_2Ti_2O_7$ would have a cubic pyrochlore crystal structure. $Sm_2Ti_2O_7$ was applied as an electronic material in the past [3, 4]. In this regard, $Er_2Ti_2O_7$ belongs to a series of rare-earth pyrochlore compounds having the general formula of $RE_2Ti_2O_7$. The spins of $RE^{3+}$ ions are located in the face centred cubic (fcc) array of corner sharing tetrahedra forming this pyrochlore lattice [5, 6]. The monoclinic structure of $La_2Ti_2O_7$ has a layered perovskite structure with monoclinic crystal system and different distances of donor-donor in different directions of the lanthanide ions, which offers the possibility of high concentration ion doping. Also, $La_2Ti_2O_7$ is an excellent host crystal for rare earth ions to produce a variety of photoluminescence properties [7, 8]. Due to excellent electro-optic and piezoelectric properties and high Curie temperature, $La_2Ti_2O_7$ has been studied as a material for electrical and optical devices [9, 10].

The aim of this study was to investigate $RE_2Ti_2O_7$ type host crystal in terms of photoluminescence and piezoelectric properties. Thus, $Nd^{3+}$ doped $La_2Ti_2O_7$, $Ce^{4+}$ doped $Sm_2Ti_2O_7$ and $Gd^{3+}$ doped $Er_2Ti_2O_7$ were selected for the experiments. The compounds were sythesized using solid state reaction method. The photoluminescence and piezoelectric properties were obtained by doping the $RE_2Ti_2O_7$ host crystal (RE: $La^{3+}$, $Sm^{4+}$ and $Er^{3+}$) with a small amount of rare earth ions ($Nd^{3+}$, $Ce^{4+}$ and $Gd^{3+}$).

## 2. Experimental

1 mol% $Nd^{3+}$ doped $La_2Ti_2O_7$, 1 mol% $Ce^{4+}$ doped $Sm_2Ti_2O_7$ and 1 mol% $Gd^{3+}$ doped $Er_2Ti_2O_7$ powders were prepared by a solid state reaction method. The starting

*E-mail: esracircir@gmail.com

© 2019. This is an open access article distributed under the Creative Commons Attribution-NonCommercial-NoDerivatives 4.0 License. (http://creativecommons.org/licenses/by-nc-nd/4.0/)

powders were weighed in nominal composition of $La_{1.98}Nd_{0.02}Ti_2O_7$, $Sm_{1.98}Ce_{0.02}Ti_2O_7$ and $Er_{1.98}Gd_{0.02}Ti_2O_7$ from $La_2O_3$ (99.99 %, Acros), $Sm_2O_3$ (99.99 %, Aldrich), $Er_2O_3$ (99.9 %, Aldrich), $Nd_2O_3$ (99.9 %, Acros), $CeO_2$ (99.95 %, Aldrich), $Gd_2O_3$ (99.9 %, Acros) and $TiO_2$ (99.95 %, Aldrich) and well mixed in an agate mortar. To determine the decomposition and the oxidation process of the powder mixtures the materials were analyzed by the simultaneous differential thermal analysis (DTA) and thermogravimetric (TG) analysis (Seiko Instruments Inc./Exstar TG/DTA 630) at a heating rate of 10 °C/min from room temperature to 1300 °C. The powder mixtures were packed into an alumina crucible and annealed in a muffle furnace in an open atmosphere. The samples were preheated at 800 °C for 3 h and then calcined from room temperature to a high temperature of 1050 °C, 1100 °C, 1200 °C, 1300 °C, 1400 °C for 24 hours. The annealed powder samples were analyzed by X-ray powder diffraction technique (XRD) with a BRUKER AXS D8 ADVANCE model X-ray diffractometer, which operated at 40 kV and 30 mA (CuK$\alpha$ radiation) in a step-scan mode (0.02 °/2θ). The microstructure and elemental analyses of the samples were performed using a LEO 440 model scanning electron microscope at an accelerating voltage of 20 kV. Photoluminescence spectra of the samples were recorded using a photoluminescence spectrophotometer (Photon Technology International (PTI), QuantaMaster$^{TM}$ 30).

For dielectric and piezoelectric measurements, aqueous slurries were prepared by adding 2 wt.% polyvinyl alcohol as a binding agent (99 % purity, Sigma-Aldrich) to the deionized water, and then 5 vol.% solids which contained $La_{1.98}Nd_{0.02}Ti_2O_7$, $Sm_{1.98}Ce_{0.02}Ti_2O_7$ and $Er_{1.98}Gd_{0.02}Ti_2O_7$ powders. The mixed samples were pressed into 10 mm diameter pellets under 250 MPa pressure by uniaxial pressing and heated at 1400 °C for 4 hours under open atmosphere to eliminate the binding agent. After this stage, the thickness and diameter of the pelletized samples were measured. The experimental and relative density of the samples were measured according to Archimedes method. The pelletized sample was coated with a silver paste (99.9 %) heated and fired at 650 °C for 1 h for the electrical measurements. The capacitance (C) and loss tangent (tanδ) were measured at 1 kHz using an LCR-meter (Hioki IM3536). An electric field of 9 to 18 kV/mm was applied to the pelletized samples in a silicon oil bath at 120 °C for 30 minutes. After 24 hours, piezoelectric charge constant ($d_{33}$) of the samples was measured by a $d_{33}$-meter. To determine Curie temperature ($T_c$) of sintered powder samples at the last heating stage, a simultaneous differential thermal analysis (DTA) and thermogravimetric (TG) analysis system was used.

## 3. Results and discussion

The TG-DTA curves of the starting materials mixture are shown in Fig. 1a, Fig. 1b and Fig. 1c. In Fig. 1, no mass loss is observed in the thermograms. It is an expected result because all starting materials were the oxide compounds. In Fig. 1a and Fig. 1c no exothermic/endothermic peaks are revealed, however, in the termogram (Fig. 1b) an endothermic peak at 1120 °C attributed to phase formation of $Sm_{1.98}Ce_{0.02}Ti_2O_7$ is observed.

The powder samples were calcined at different times and temperatures, i.e. from room temperature up to 1050 °C, 1100 °C, 1200 °C, 1300 °C, 1400 °C for 24 hours. After the calcination processes, the XRD analysis was performed. The all peaks for $La_{1.98}Nd_{0.02}Ti_2O_7$ calcined at 1400 °C, can be attributed to the $La_2Ti_2O_7$ phase (PDF Card No. 01-076-3299), revealing that $Nd^{3+}$ ions have been efficiently incoroprated into the host crystal $La_2Ti_2O_7$. The strongest peak of the $La_{1.98}Nd_{0.02}Ti_2O_7$ structure is centered at $2\theta = 29.7801°$ and it corresponds to the crystalline plane with Miller indices of (2 1 2). $La_{1.98}Nd_{0.02}Ti_2O_7$ has a monoclinic system with the unit cell parameters a = 7.80896 Å, b = 5.54608 Å, c = 13.01425 Å, $\alpha = 90°$, $\beta = 98.658°$, $\gamma = 90°$. Fig. 2b presents the XRD pattern of $Sm_{1.98}Ce_{0.02}Ti_2O_7$. The sharpest diffraction peaks at $2\theta$ values of 14.7°, 28.6°, 30.3°, 35.4°, 38.2°, 50.5° and 60.2° indicate the planes (1 1 1), (3 1 1), (2 2 2), (4 0 0), (3 3 1), (4 4 0) and (6 2 2), respectively and are consistent with PDF Card No. 01-072-9772. This confirms the formation of $Sm_2Ti_2O_7$ and $Ce^{4+}$ doping

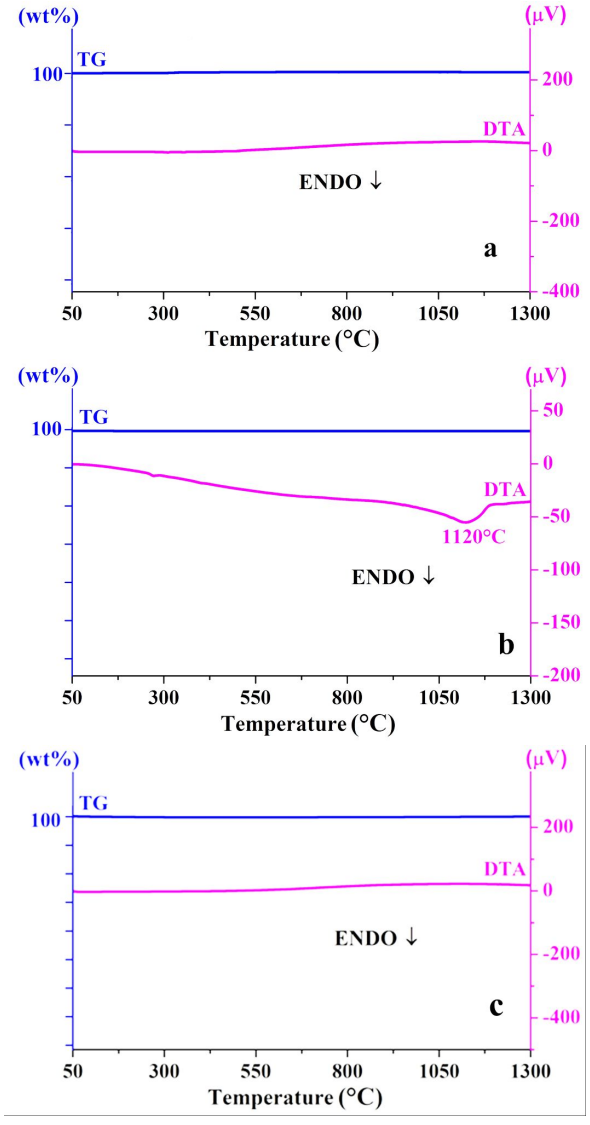



Fig. 1. TG/DTA curves of starting materials mixtures of (a) $La_{1.98}Nd_{0.02}Ti_2O_7$, (b) $Sm_{1.98}Ce_{0.02}Ti_2O_7$, (c) $Er_{1.98}Gd_{0.02}Ti_2O_7$.

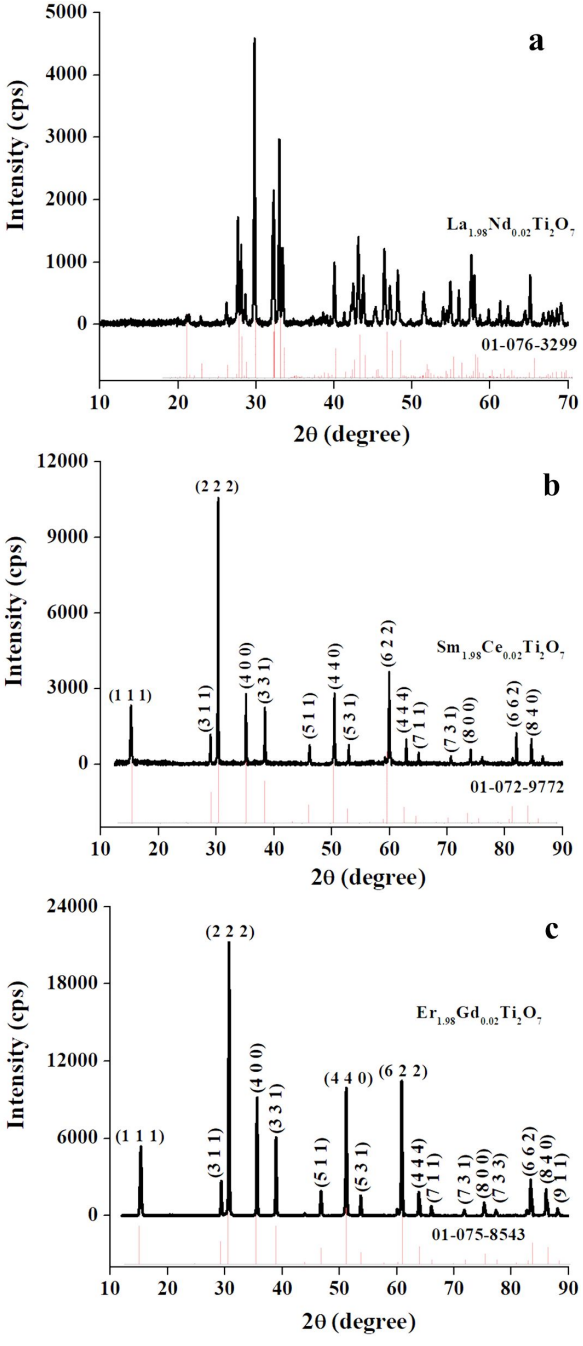



Fig. 2. XRD patterns of (a) $La_{1.98}Nd_{0.02}Ti_2O_7$, (b) $Sm_{1.98}Ce_{0.02}Ti_2O_7$ and (c) $Er_{1.98}Gd_{0.02}Ti_2O_7$ calcined at 1400 °C for 24 h.

into $Sm_2Ti_2O_7$ host crystal. $Sm_{1.98}Ce_{0.02}Ti_2O_7$ has a cubic crystal system with unit cell parameters a = b = c 10.231 Å, $\alpha = \beta = \gamma = 90°$. Fig. 2c shows the XRD pattern of $Er_{1.98}Gd_{0.02}Ti_2O_7$. It is shown that the XRD pattern of $Er_{1.98}Gd_{0.02}Ti_2O_7$ is in a good agreement with the perfect pyrochlore, PDF Card No. 01-075-8543. The cubic unit cell parameters of $Er_{1.98}Gd_{0.02}Ti_2O_7$ are a = b = c = 10.0965 Å, $\alpha = \beta = \gamma = 90°$.

The SEM images of the $La_{1.98}Nd_{0.02}Ti_2O_7$, $Sm_{1.98}Ce_{0.02}Ti_2O_7$ and $Er_{1.98}Gd_{0.02}Ti_2O_7$ powders prepared by solid state reaction are shown in Fig. 3. The grain size distribution range is of 0.6 μm to 4.0 μm and it reveals the polycrystalline nature of the material. The EDX analysis does not show any impurity atoms. The difference between

the calculated and observed percentages of the elements is typical of polycrystalline samples (Fig. 4).

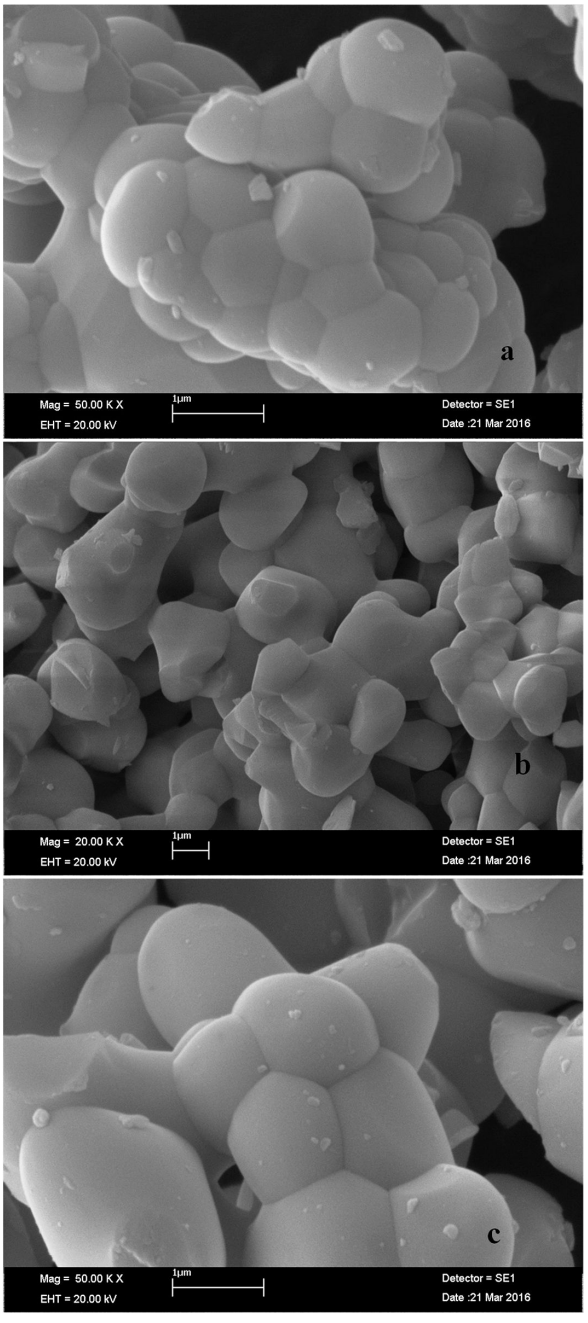



Fig. 3. SEM images of (a) $La_{1.98}Nd_{0.02}Ti_2O_7$, (b) $Sm_{1.98}Ce_{0.02}Ti_2O_7$ and (c) $Er_{1.98}Gd_{0.02}Ti_2O_7$.

Fig. 5a shows the excitation and emission spectra of $La_{1.98}Nd_{0.02}Ti_2O_7$. It can be seen that the excitation and emission peaks occur at 300 nm

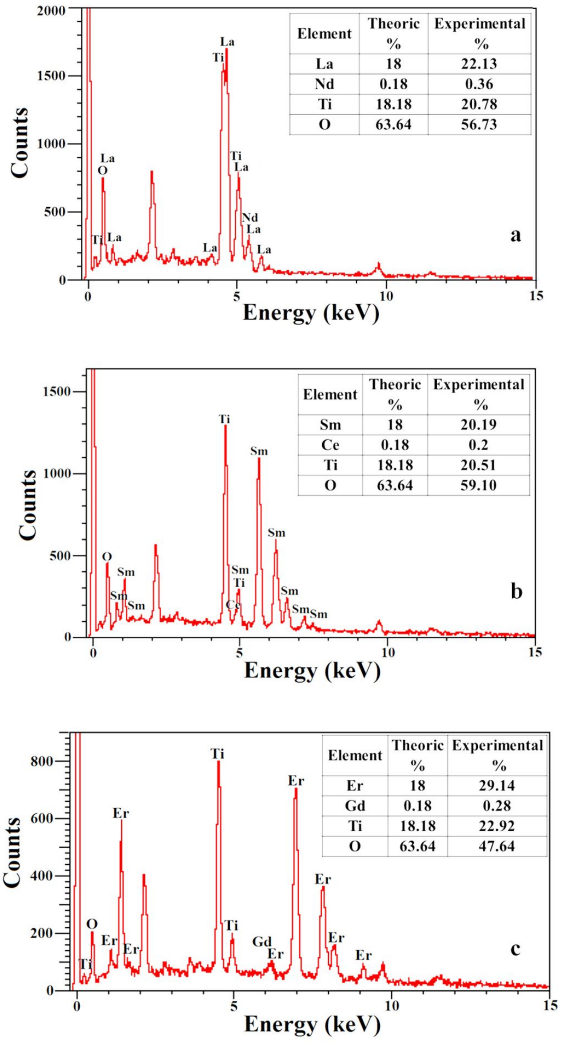



Fig. 4. EDX analysis results of (a) $La_{1.98}Nd_{0.02}Ti_2O_7$, (b) $Sm_{1.98}Ce_{0.02}Ti_2O_7$ and (c) $Er_{1.98}Gd_{0.02}Ti_2O_7$.

and 612 nm, respectively. $La^{3+}$ ions have a [Xe] $^4f_0$ inert gas configuration symbolized by a $^1S_0$ ground state. Excited states can be caused by p $\rightarrow$ d transition leading to the electronic configuration $5s^25p^55d^1$ which gives rise to the triplet $^3P_1$, $^3D_2$ and $^3F_3$ states and the singlet $^1P_1$, $^1D_2$ and $^1F_3$ states. The excited state of $La^{3+}$ ion results from p $\rightarrow$ d transition, and the crystal field surrounding the ion is approximated by an $O_h$ field. The energy transition of $La^{3+}$ arises from $^1S_0 \rightarrow {}^1F_3$ ($\sim$300 nm). The $La^{3+}$ ions with unfilled 4f orbitals act as a sensitizer and enhance the emission

of $Ti^{3+}$. The observed emission may be attributed to $Ti^{3+}$ center in the $La_2Ti_2O_7$ which is enhanced by the presence of $La^{3+}$ ions. It has been reported earlier that the transition metal activator, $Ti^{3+}$ ion, has spectral stimulated emission (SE) at about 611 nm ($^2E \rightarrow {}^2T_2$). The ions that do not possess 4f electrons are reported to have no electronic energy levels that can induce excitation and luminescence processes in or near the visible region. However, the emission peak observed at 612 nm is sharp and it can be attributed to the unfilled 4f orbital of the RE (La) added [11].

Trivalent samarium with $^4f_5$ configuration has complex energy levels and various possible transitions between f $\rightarrow$ f levels. The transitions between f levels have high selectivity and sharp line spectra. The excitation and emission spectra of $Sm_{1.98}Ce_{0.02}Ti_2O_7$ are shown in Fig. 5b. The broad excitation band located at 368 originates from $^6H_{5/2} \rightarrow {}^4D_{3/2}$ which are attributed to the f $\rightarrow$ f forbidden transitions of $Sm^{3+}$. The emission spectrum of $Sm_{1.98}Ce_{0.02}Ti_2O_7$ exhibits two obvious maxima located at 574 nm and 619 nm, being assigned to transitions from the excited $^4G_{5/2}$ state to $^6H_J$ (J = 5/2, 7/2) levels of the $Sm^{3+}$ [12–15].

Fig. 5c shows excitation and emission spectra of $Er_{1.98}Gd_{0.02}Ti_2O_7$. The excitation spectrum consists of a broad band with two maxima at 299 nmn and 364 nm. These maxima belong to intra-4f-shell transitions of $Er^{3+}$ from the ground state $^4I_{15/2}$ to higher energy levels, $^2K_{13/2}$ and $^4G_{9/2}$. In the emission spectrum, a broad band with one maximum at 523 nm is observed and attributed to the transition from the $^2H_{11/2}$ state to the $^4I_{15/2}$ ground state of $Er^{3+}$ [16, 17].

Decay time curves of $La_{1.98}Nd_{0.02}Ti_2O_7$ (for emission of $La^{3+}$ ion at 612 nm, $\lambda_{ex}$: 300 nm), $Sm_{1.98}Ce_{0.02}Ti_2O_7$ (for $^4G_{5/2} \rightarrow {}^6H_{7/2}$ transition of $Sm^{3+}$ ion at 619 nm, $\lambda_{ex}$: 368 nm) and $Er_{1.98}Gd_{0.02}Ti_2O_7$ (for $^2H_{11/2} \rightarrow {}^4I_{15/2}$ transition of $Er^{3+}$ ion at 523 nm, $\lambda_{ex}$: 299 nm) are shown in Fig. 6a, Fig. 6b and Fig. 6c. The decay curves are simulated and decay times are calculated using the single exponential function:

$$I(t) = I_0 \cdot exp(-t/\tau) \quad (1)$$

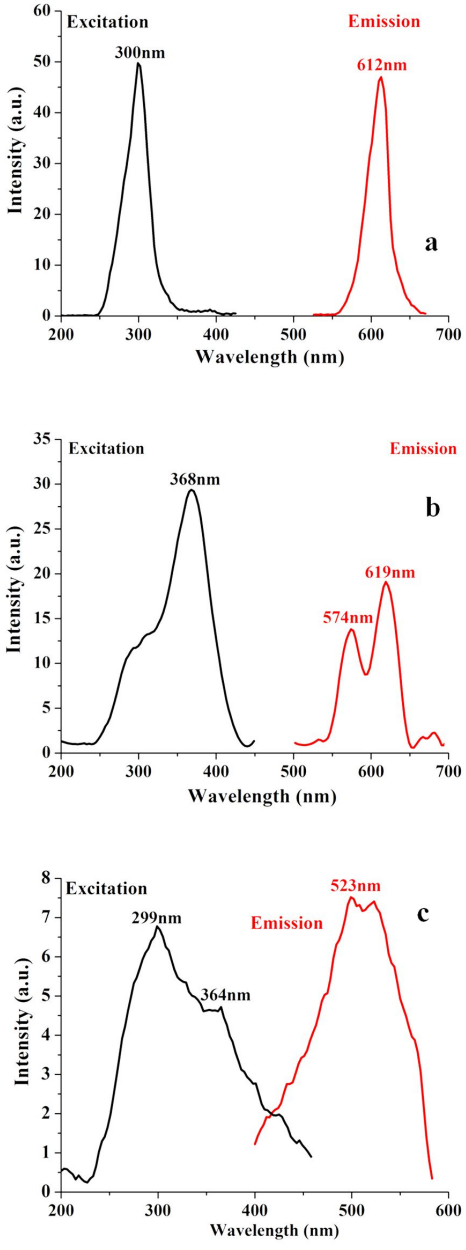



Fig. 5. The excitation and emission spectra of (a) $La_{1.98}Nd_{0.02}Ti_2O_7$ ($\lambda_{em}$: 612 nm, $\lambda_{ex}$: 300 nm), (b) $Sm_{1.98}Ce_{0.02}Ti_2O_7$ ($\lambda_{em}$: 619 nm, $\lambda_{ex}$: 368 nm) and (c) $Er_{1.98}Gd_{0.02}Ti_2O_7$ ($\lambda_{em}$: 523 nm, $\lambda_{ex}$: 299 nm).

where $I_0$ is the initial intensity and $\tau$ is the decay time constant. According to the fitting results, the decay times are 5.224 μs, 2.0 μs and 6.022 μs for $La_{1.98}Nd_{0.02}Ti_2O_7$, $Sm_{1.98}Ce_{0.02}Ti_2O_7$ and $Er_{1.98}Gd_{0.02}Ti_2O_7$ phosphors, respectively.

Table 1. Thickness t, diameter ∅ and relative densities of the pelletized samples.

| | Thickness t [mm] | Diameter ∅ [cm] | Experimental density $\rho_{ex}$ [g/cm$^3$] | Theoretical density $\rho_{teo}$ [g/cm$^3$] | Relative density $\rho_{re}$ |
|---|---|---|---|---|---|
| $La_{1.98}Nd_{0.02}Ti_2O_7$ | 0.94 | 1.006 | 5.92 | 5.729 | 0.97 |
| $Sm_{1.98}Ce_{0.02}Ti_2O_7$ | 1.1 | 0.9 | 6.3 | 6.309 | 1.00 |
| $Er_{1.98}Gd_{0.02}Ti_2O_7$ | 0.9 | 1.0 | 6.95 | 7.138 | 1.00 |

Table 2. Capacitance C, dielectric constant $E_r$, loss tangent tanδ, piezoelectric charge constant $d_{33}$ and Curie temperature $T_c$ of the samples.

| | Capacitance C [F] | Dielectric constant $E_r$ | Loss tangent, tanδ [%] | Piezoelectric charge constant $d_{33}$ [pC/N] | Curie temperature $T_c$ [°C] |
|---|---|---|---|---|---|
| $La_{1.98}Nd_{0.02}Ti_2O_7$ | 14.74 | 12 | 2.15 | 0.53 | 1558 |
| $Sm_{1.98}Ce_{0.02}Ti_2O_7$ | 22.52 | 36 | 1.22 | 0.5 | 1574 |
| $Er_{1.98}Gd_{0.02}Ti_2O_7$ | 16.3 | 21.12 | 3.6 | 0.5 | 1560 |

For the dielectric and piezoelectric measurements, thickness (t) and diameter (∅) of the pelletized samples were measured and the densities were calculated using the Archimedes method. The dimensions and densities are shown in Table 1. After that, the capacitance C and loss tangent tanδ of pelletized samples coated with silver paste were measured and dielectric constant $E_r$ was calculated using the equation 2:

$$E_r = C \cdot t / A \cdot E_0 \tag{2}$$

Then, the pelletized samples were exposed to an electric field of 9 kV/mm to 18 kV/mm in a silicon oil bath at 120 °C for 30 minutes. After 24 hours, piezoelectric charge constant $d_{33}$ of all samples was measured by a $d_{33}$-meter. Curie temperature $T_c$ of sintered powder samples annealed at 1400 °C for 4 h was determined using a TG/DTA system (Fig. 7). The first endotermic peak temperature in the termograms belonging to any phase transition is attributed to Curie temperature because the material loses its piezoelectric properties at temperatures above Curie temperature [18, 19]. The capacitance C, dielectric constant $E_r$, loss tangent tanδ, piezoelectric charge constant $d_{33}$ and Curie temperature of the pelletized samples are listed in Table 2. When comparing the electrical properties, $Sm_{1.98}Ce_{0.02}Ti_2O_7$ has the largest dielectric constant. All these materials have similar piezoelectric constant and Curie temperature.

## 4. Conclusions

In this work, we sythesized and characterized multifinctional materials $La_{1.98}Nd_{0.02}Ti_2O_7$, $Sm_{1.98}Ce_{0.02}Ti_2O_7$ and $Er_{1.98}Gd_{0.02}Ti_2O_7$. The materials have photoluminescent and piezoelectric properties. The $^4G_{5/2} \rightarrow {}^6H_{7/2}$ (619 nm) transition of $Sm^{3+}$ has the strongest intensity and can be applied to orange-red emitting display materials. In particular, the emission peaks are centered in the green region, and these color coordinates are desirable. Such partial emission in the green region only with favorable color coordinates is very rare for $Er^{3+}$ other than in inorganic oxide host, where emission with moderate intensity is observed between 500 nm and 700 nm. Additionally, $La_{1.98}Nd_{0.02}Ti_2O_7$, $Sm_{1.98}Ce_{0.02}Ti_2O_7$ and $Er_{1.98}Gd_{0.02}Ti_2O_7$ have high Curie temperature which is 1558 °C, 1574 °C and 1560 °C, respectively. The obtained results indicate that the $La_{1.98}Nd_{0.02}Ti_2O_7$, $Sm_{1.98}Ce_{0.02}Ti_2O_7$ and $Er_{1.98}Gd_{0.02}Ti_2O_7$ are multifunctional smart material with promising red and green PL useful for optoelectronic applications.

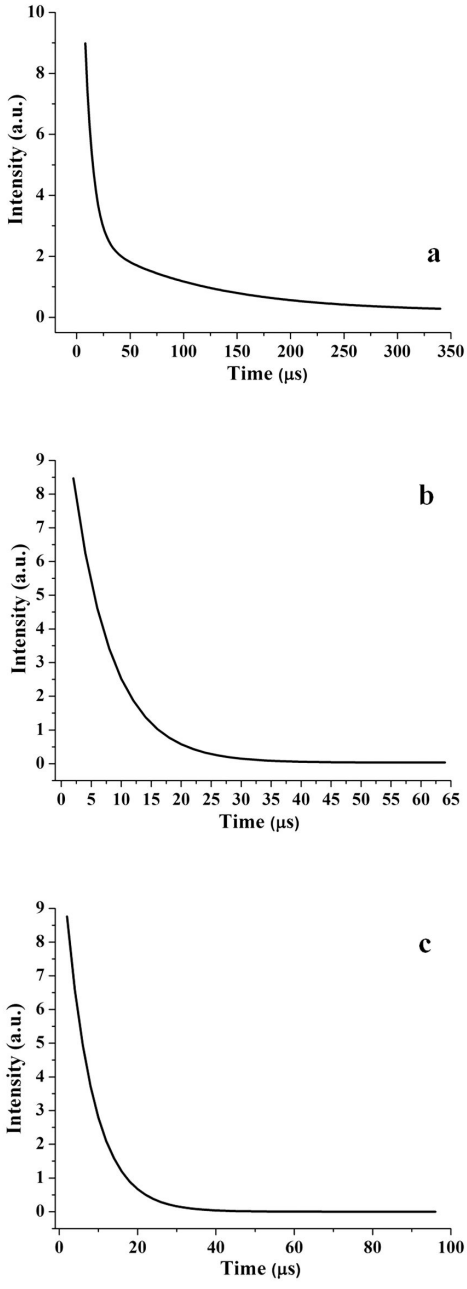



Fig. 6. Decay curves of (a) $La_{1.98}Nd_{0.02}Ti_2O_7$ ($\lambda_{em}$: 612 nm), (b) $Sm_{1.98}Ce_{0.02}Ti_2O_7$ ($\lambda_{em}$: 619 nm) and (c) $Er_{1.98}Gd_{0.02}Ti_2O_7$ ($\lambda_{em}$: 523 nm).

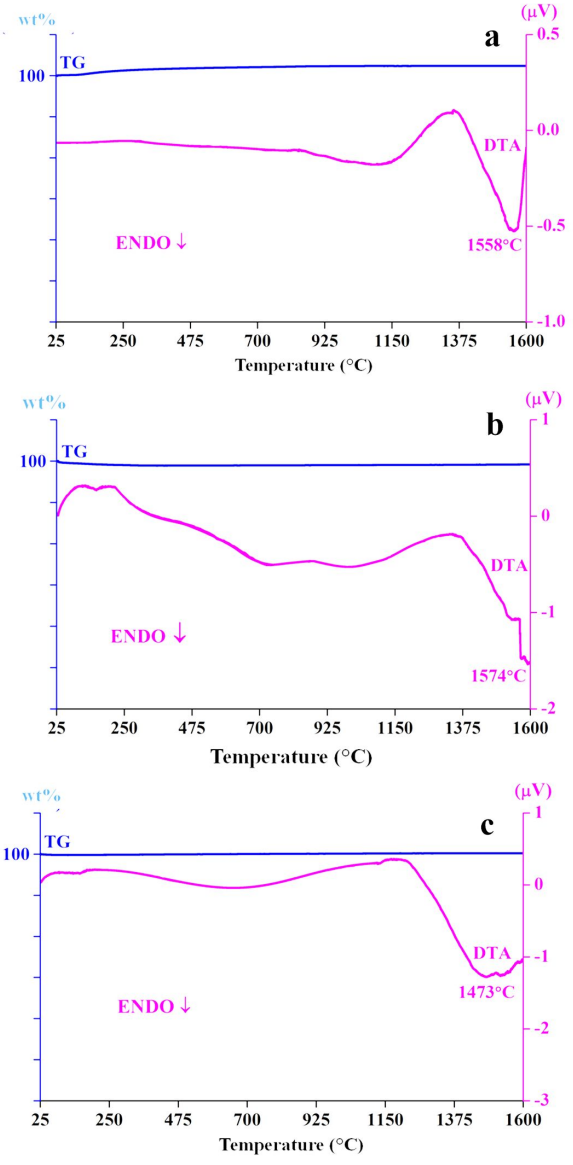



Fig. 7. TG/DTA curves and Curie temperature of (a) $La_{1.98}Nd_{0.02}Ti_2O_7$, (b) $Sm_{1.98}Ce_{0.02}Ti_2O_7$ and (c) $Er_{1.98}Gd_{0.02}Ti_2O_7$.

## Acknowledgements

The authors would like to thank the TUBITAK (The Scientific and Technological Research Council of Turkey) for the support to the Project Numbered 114Z438.

## References

[1] EWING R.C., WEBER W.J., LIAN J., *J. Appl. Phys.*, 95 (2004), 5929.

[2] SUBRAMANIAN M.A., ARAVAMUDAN G., SUBBA RAO G.V., *Prog. Solid State Chem.*, 15 (1983), 55.

[3] JAFAR M., SENGUPTA P., ACHARY S.N., TYAGI A.K., *J. Eur. Ceram. Soc.*, 34 (2014), 4373.

[4] RABANAL M.E., VÁREZ A., AMADOR U., DOMPABLO E.A., GARCIA-ALVARADO F., *J. Mater. Process. Technol.*, 92 – 93 (1999), 529.

[5] MOESSNER R., *J. Phys.*, 79 (2001), 1283.

[6] RAMIREZ A.P., *Annu. Rev. Mater. Sci.*, 24 (1994), 453.
[7] DIALLO P.T., BOUTINAUD P., MAHIOU R., COUSSEINS J.C., *J. Alloy. Compd.,* 275 – 277 (1998), 307.
[8] YANG H.H., CHENG H., TANG Y.G., LU Z.G., *Am. Ceram. Soc.*, 92 (2009), 931.
[9] TITOV Y.A., SYCH A.M., MARKIV V.Y., BELYAVINA N.M., KAPSHUK A.A., YASCHUK V.P., *J. Alloy. Compd.,* 316 (2001), 309.
[10] LI A.D., WANG Y.J., HUANG S., CHENG J.B., WU D., MING N.B., *J. Cryst. Growth*., 268 (2004), 198.
[11] LYJO J.K., DAYAS K.R., DAMODAR S., KRISHNAN B., KRISHNANKUTTY K., NAMPOORI V.P.N., RADHAKRISHNAN P., *Spectrochim. Acta A,* 71 (2008), 1281.
[12] LI Y.-C., CHANG Y.-H., LIN Y.-F., CHANG Y.-S., LIN Y.-J., *J. Alloy. Compd.,* 439 (2007), 367.
[13] DORDEVIC V., NIKOLIC M.G., ANTIC Ž., MITRIC M., DRAMICANIN M.D., *Acta Phys. Pol. A*, 120 (2011), 303.
[14] NARESH V., BUDDHUDU S., *J. Lumin.,* 147 (2014), 63.
[15] DENG H., ZHAO Z., WANG J., HEI Z., LI M., NOH H.M., JEONG J.H., YU R., *J. Solid State Chem.,* 228 (2015), 110.
[16] LI Y.-C., CHANG Y.-H., LIN Y.-F., LIN Y.-J., *Appl. Phys. Lett.,* 89 (2006), 081110.
[17] LI A., SUN L., ZHENG Z., WU W., LIU W., YANG Y., LU T., SU W., *J. Lumin.,* 128 (2008), 239.
[18] MANI M.K., VIOLA G., HALL J., GRASSO S., REECE M.J., *J. Magn. Magn. Mater.*, 382 (2015), 202.
[19] FERK G., DROFENIK M., LISJAK D., HAMLER A., JAGLIČIĆ Z., MAKOVEC D., *J. Magn. Magn. Mater.*, 350 (2015), 124.

*Received 2018-12-19*
*Accepted 2019-04-23*